Multiple Charge Transfer States in Donor−Acceptor Heterojunctions with Large Frontier Orbital Energy Offsets

Saeed-Uz-Zaman Khan,[†] Giacomo Londi,[‡] Xiao Liu,[†] Michael A. Fusella,[†] Gabriele D'Avino,[§] Luca Muccioli,[∥,⊥] Alyssa N. Brigeman,[#] Bjoern Niesen,[∇] Terry Chien-Jen Yang,[∇] Yoann Olivier,[‡] Jordan T. Dull,[†] Noel C. Giebink,[#] David Beljonne,[‡] and Barry P. Rand*,[†,○]

[†]Department of Electrical Engineering, Princeton University, Princeton, New Jersey 08544, United States

[‡]Laboratory for Chemistry of Novel Materials, University of Mons, Place du Parc 20, 7000 Mons, Belgium

[§]Institut Néel, CNRS and Grenoble Alpes University, F-38042 Grenoble, France

[∥]Dipartimento di Chimica Industriale "Toso Montanari", Università di Bologna, I-40136, Bologna, Italy

[⊥]Institut des Sciences Moléculaires, UMR 5255, University of Bordeaux, F-33405 Talence, France

[#]Department of Electrical Engineering, The Pennsylvania State University, University Park, Pennsylvania 16802, United States

[∇]Photovoltaics and Thin-Film Electronics Laboratory, Institute of Microengineering (IMT), Ecole Polytechnique Fédérale de Lausanne (EPFL), Maladière 71, Neuchâtel 2000, Switzerland

[○]Andlinger Center for Energy and the Environment, Princeton University, Princeton, New Jersey 08544, United States

S *Supporting Information*

ABSTRACT: In this work, we demonstrate several organic amorphous donor−acceptor systems that exhibit sub-bandgap features over a more than 2 eV spectral range. An in-depth study of one of these systems, NPB:HAT-CN (NPB is *N,N′*-di(1-naphthyl)-*N,N′*-diphenyl-(1,1′-biphenyl)-4,4′-diamine and HAT-CN is 1,4,5,8,9,11-hexaazatriphenylenehexacarbonitrile), reveals that the broad sub-bandgap features are attributed to multiple electronic charge transfer (CT) state transitions, broadened by energetic disorder sourcing from the fluctuations of intramolecular conformations and by the disordered intermolecular environment. These unique CT features originate from an unconventional donor and acceptor selection that reveals new insight about photocurrent generation and nonradiative recombination. Unlike materials employed in high performing organic solar cells, the materials studied here feature large optical energy gaps with very large frontier orbital energy level offsets, creating high bandgap devices with low open-circuit voltage. In addition to multiple electronic CT levels, we reveal that the internal quantum efficiency of these multiple CT transitions is not constant but photon energy dependent and with photoluminescence that originates primarily from the second lowest electronic CT state implying slow (relative to radiative and nonradiative rates) internal conversion within the CT manifold. Overall, this class of donor−acceptor pairs provides an opportunity to probe CT states in unique ways to potentially unravel their role in carrier generation−recombination and energy loss mechanisms.
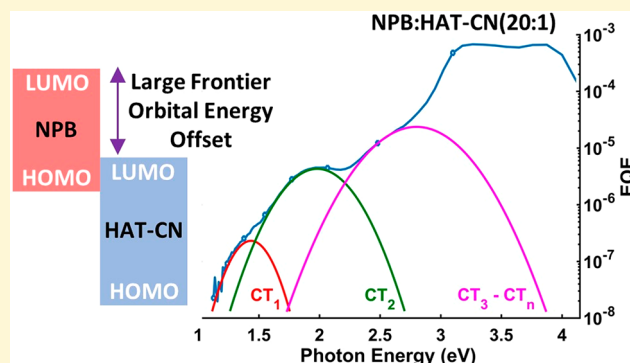
INTRODUCTION

With more than 15% power conversion efficiency recently achieved[1] and coupled with the ability to be grown on flexible substrates on a large scale with low-cost fabrication techniques, organic solar cells are making a strong case for energy conversion applications. Most advances in power conversion efficiency are the result of impressive material and interface engineering and innovation. However, due to the lack of a complete understanding and consensus of carrier generation and recombination processes as well as loss mechanisms at charge generating donor−acceptor (D-A) interfaces,[2] the actual limits of organic solar cell performance remain unknown. In this context, intermolecular charge transfer

(CT) excitations at D−A interfaces play an important role in the photophysical processes and energy losses of organic solar cells.[3−6] In order to understand how carrier generation and recombination are affected by CT states, a better comprehension of their origin and energetic distribution is crucial. More specifically, some key issues that are currently under inquiry include whether the carrier dissociation efficiency

depends on incident photon energy[3,7−9] or not,[10,11] the origin of the broadening of the CT state line-shape (static and dynamic disorder),[6,12−15] the possibility and origin of multiple CT states (electronic, vibronic, or morphology induced),[16−20] and reciprocity of CT state absorption and emission spectra (thermal and nonthermal state distribution).[21−24] One step toward addressing these issues is to identify organic D−A systems that display unique CT state characteristics, in order to probe their CT state energies in novel ways.

In fact, the optical signature of CT states is often buried in the background signal of much more strongly absorbing Frenkel (i.e., intramolecular or localized) excitons.[25] While techniques that exploit anisotropy can reveal the CT state region underneath this background,[26] such methods are effective only in the presence of crystalline order granting sufficient dipole alignment at the D−A interface. To overcome those experimental limitations, in this work, we present several wide bandgap D−A systems consisting of both small molecule and polymer organic semiconductors with large frontier orbital energy offsets (i.e., large energetic driving force for charge separation), resulting in ultrabroad CT state spectra. Despite varying molecular structure and energetics, these large offset heterojunctions display complex CT features that span more than 2 eV, well outside the Frenkel exciton region.

We then investigate the nature of these sub-bandgap features in detail through a comprehensive experimental and computational study of the D−A system of NPB:HAT-CN (NPB is *N,N′*-di(1-naphthyl)-*N,N′*-diphenyl-(1,1′-biphenyl)-4,4′-diamine and HAT-CN is 1,4,5,8,9,11-hexaazatriphenylenehexacarbonitrile). Ultrasensitive sub-bandgap absorption spectra reveal the existence of low energy CT states that do not contribute to photocurrent as probed via spectrally resolved external quantum efficiency (EQE) measurements, despite having comparable (relative to higher energy CT states) absorption strength. Through spectral absorption, EQE, photoluminescence (PL), electroluminescence (EL) measurements and combined molecular dynamics (MD) simulations and electronic structure calculations, we confirm the existence of multiple electronic CT states at these heterojunctions, which are broadened by nanoscale conformational and electrostatic variations. Finally, EQE measurements under applied voltage bias indicate that internal quantum efficiency (IQE) is strongly dependent on incident photon energy in these large offset heterojunction solar cells, providing an example of nonconstant IQE similar to previous reports on some polymer blends,[27,28] but contrary to observations in most high-performance solar cells.[10] We attribute the reduced IQE of low energy CT states to an efficient nonradiative recombination pathway, whose rate increases with decreasing CT energy as a result of larger vibrational overlap (also known as the energy gap law).[29]

One of the major challenges in designing high-performance organic solar cells is indeed the reduction of CT-mediated nonradiative recombination losses.[30,31] Comprehensive experimental studies have introduced design rules that mandate smaller frontier orbital energy offsets to minimize nonradiative energy losses,[32] in compliance with the energy gap law of organic materials.[30,33] This nonradiative loss component is hypothesized to be intrinsic to organic semiconductors, stemming from the increasing Franck−Condon overlap between CT and the ground state when the difference between their electronic energies decreases, an aspect that is distinct from defect and surface recombination induced nonradiative

losses.[29] The high frontier orbital energy offset materials studied in this work yields low-energy CT states that are prone to efficient nonradiative recombination because of large vibrational overlap, leading to a much larger intrinsic energy loss component and an opportunity to test hypotheses about nonradiative losses.

■ RESULTS AND DISCUSSION

In this work, we demonstrate six D−A systems that exhibit approximately 2 eV wide subgap spectra, by blending wide optical energy gap materials with large offset energies. As donors, we used the small molecules NPB, 4,4′,4″-tris[(3-methylphenyl)phenylamino]triphenylamine (m-TDATA), 4,4′-cyclohexylidenebis[*N,N*-bis(4-methylphenyl)-benzenamine] (TAPC), *N,N′*-bis(3-methylphenyl)-*N,N′*-diphenylbenzidine (TPD), and the polymer poly(9-vinylcarbazole) (PVK). As acceptors, we employed either HAT-CN or 1,4,5,8-naphthalenetetracarboxylic dianhydride (NTCDA). All donor molecules here have optical gaps greater than 3 eV, while the acceptor molecules have an approximately 4 eV optical gap and large electron affinity (EA; see Table S1). The energy gap between the highest occupied molecular orbital (HOMO) of the donor and lowest unoccupied molecular orbital (LUMO) of the acceptor is therefore significantly smaller than in typical high-performing organic solar cells. This leads to low open-circuit voltage (V_{OC}) and, notably, broad sub-bandgap spectral features, as shown in Figure 1 for coevaporated bulk heterojunctions (BHJs), except
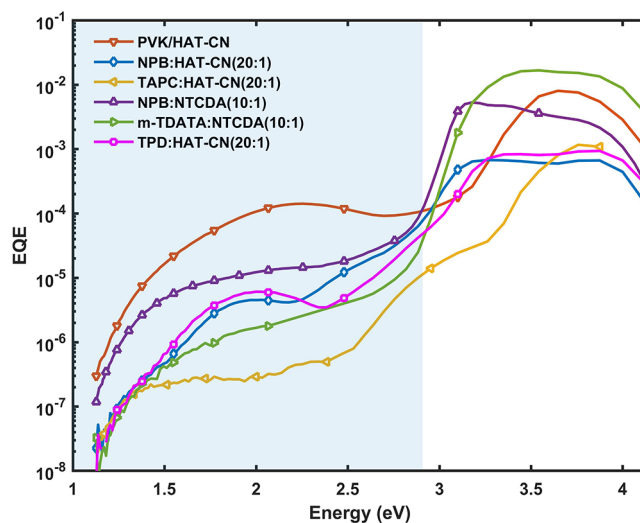
Figure 1. External quantum efficiency (EQE) spectra of organic bulk and planar heterojunction solar cells, exhibiting broad CT spectra (shaded region) extending to approximately 1.1 eV.

for the sequentially deposited PVK/HAT-CN planar heterojunction (PHJ). Interestingly, the EQE features of all devices do not extend below approximately 1.1 eV, despite considerable variations in their CT energy gap, ionization potential $(IP)_{donor} − EA_{acceptor}$, as inferred from measurements on the individual materials.

To understand the nature of the broad sub-bandgap EQE features, we have conducted an in-depth investigation on the NPB:HAT-CN D−A system. The EQE spectra for NPB:HAT-CN BHJs with various D:A ratios are shown in Figure 2. For the 20:1 D:A blend, there are three distinct sub-bandgap EQE features centered around 1.4, 2.0, and 2.8 eV that match the
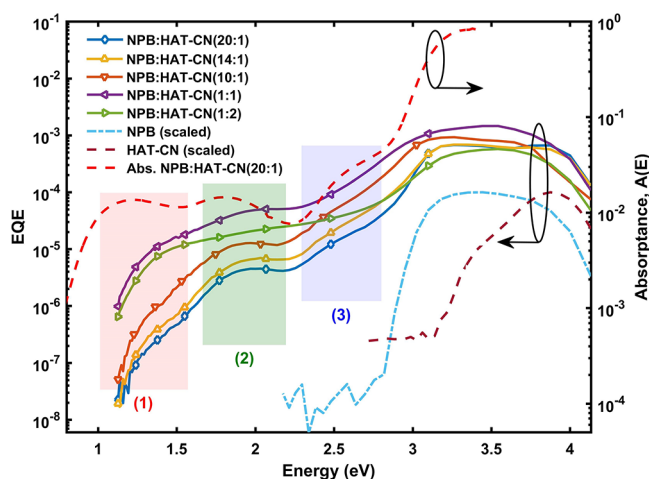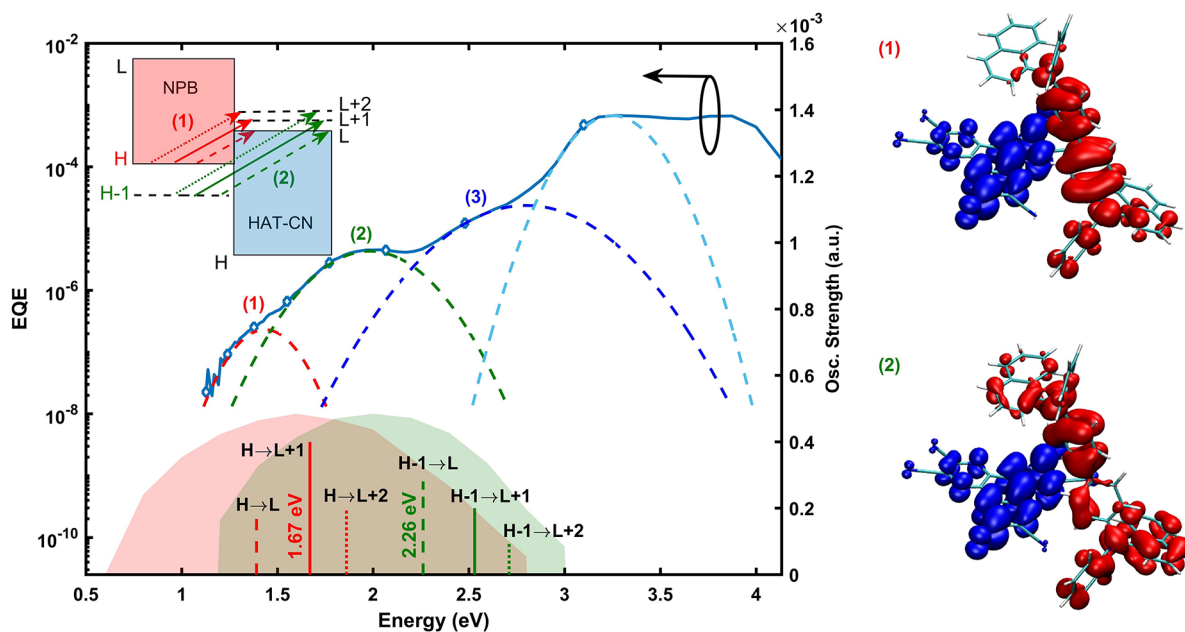
Figure 2. External quantum efficiency (EQE) spectra of NPB:HAT-CN bulk heterojunctions with various D:A blend ratios (solid lines). The HAT-CN concentration was varied from 4.5 vol % (20:1 blend) to 67 vol % (1:2 blend). The sky blue and maroon dashed lines are scaled EQE from single layers of NPB and HAT-CN, respectively. The red (1), green (2), and blue (3) colored boxes designate the three primary CT features in this system. The red dashed line is the absorptance of a NPB:HAT-CN (20:1) film measured by photothermal deflection spectroscopy.

spectrum can then be attributed to photocurrent generation from direct CT absorption.

The comparison to a control device with NPB p-doped by the very strong oxidant MoO_3 (see Figure S1) provides additional information about the subgap features of NPB:HAT-CN BHJs. The PDS spectrum of MoO_3-doped NPB shows two distinct polaron absorption peaks located at 0.9 and 2.6 eV, which are in agreement with the NPB polaron peaks observed through charge modulation spectroscopy reported in the literature.[34] However, these polaron peaks do not match with the NPB:HAT-CN PDS (dashed red line) features in Figure 2, with peaks at 1.2, 1.8, and 2.5 eV. The low-energy tail of the PDS spectrum seems to suggest the presence of the NPB cation in this blend, i.e., of a slight doping. The low energy feature in NPB:HAT-CN (20:1) PDS and EQE spectra has a ~0.3 eV discrepancy with the low energy NPB polaron peak and we can safely assert that the low energy polaron peak is not contributing to photocurrent generation. However, we cannot exclude that the feature around 2.5−2.8 eV in the EQE and PDS spectra of NPB:HAT-CN presents a contribution from the corresponding polaron peak observed in the PDS spectrum of MoO_3-doped NPB. An additional hint of the special role played by HAT-CN is that the EQE of MoO_3-doped NPB single layer devices (Figure S1) shows no subgap signal.

The EQE spectra of NPB:HAT-CN BHJs change with the D:A mixing ratio, as shown in Figure 2. As the HAT-CN concentration increases from 4.5 vol % (i.e., NPB rich) to 67 vol % (i.e., HAT-CN rich), an increase of D−A interfacial volume leads to an increase of overall CT state EQE,[35,36]

absorption peaks in the photothermal deflection spectroscopy (PDS) spectrum, except that the lowest energy EQE shoulder is cut off at around 1.1 eV. All three features in the EQE

Figure 3. External quantum efficiency (EQE) spectrum of a NPB:HAT-CN (20:1; blue solid line) device. Four Gaussian functions fit to the EQE spectrum, yielding CT_1 (dashed red line, center: 1.44 eV; fwhm: 0.31 eV), CT_2 (dashed green line, center: 1.98 eV; fwhm: 0.50 eV), CT_3 (dashed blue line, center: 2.78 eV; fwhm: 0.65 eV), and the NPB Frenkel exciton (dashed light blue line, center: 3.27 eV; fwhm: 0.37 eV), are also shown. The red and green shaded Gaussians established from combining MD simulations and electronic structure calculations correspond to the energetic distribution of CT_1 and CT_2 centered at 1.62 eV and 2.01 eV, respectively. The red and green delta lines represent CT energies calculated from TD-DFT of an NPB-HAT-CN dimer, among which are two primary ones at 1.67 eV and 2.26 eV, respectively, with their electron (blue) and hole (red) densities shown at the right. The inset displays transitions from NPB HOMO (H) and HOMO−1 (H-1) to HAT-CN LUMOs (L, L+1, and L+2), which contribute mostly to the hole−electron density of the lowest CT states. The CT_3 region represents higher energy CT states, associated with transitions from deeper HOMO levels of NPB to higher energy LUMO levels of HAT-CN, along with some contribution from NPB polaron (cation) absorption.

peaking for the 1:1 blend, while the three distinct CT features gradually merge. The concomitant increase in sub-bandgap EQE, as the D−A blend goes from nonequimolar to equimolar ratios, provides further support that the sub-bandgap spectra of NPB:HAT-CN BHJs indeed originate from CT state absorption.[35] At the same time, V_{OC}'s of these devices decrease significantly (Figure S2, Table S2) with increasing HAT-CN concentration. The decrease of V_{OC} could be due both to the increase in CT-mediated recombination at the NPB-HAT-CN interface[23,35,36] and to the increasing population of NPB cations and HAT-CN anions that are introduced by charge transfer (i.e., doping). Temperature dependent current density−voltage measurements (Figure S3a) show that V_{OC} increases continuously as temperature decreases, indicating the presence of strong recombination at room temperature for both 20:1 and 1:2 NPB:HAT-CN blends. However, the dark current density−voltage characteristics (Figure S3b) display a sharp increase in reverse bias current with increasing HAT-CN concentration, implying that decreased shunt resistance is the dominant factor for the decrease in V_{OC}. Atomic force microscope images of 20:1 and 1:2 NPB:HAT-CN blend films (Figure S3c) confirm that both films are pinhole free, have similar r.m.s. surface roughness (2.63 and 3.35 nm, respectively), and follow the morphology of the ITO underneath. These collective observations indicate that the decreased shunt resistance is likely to originate from increased doping, rather than morphological changes of the films with higher HAT-CN concentration.
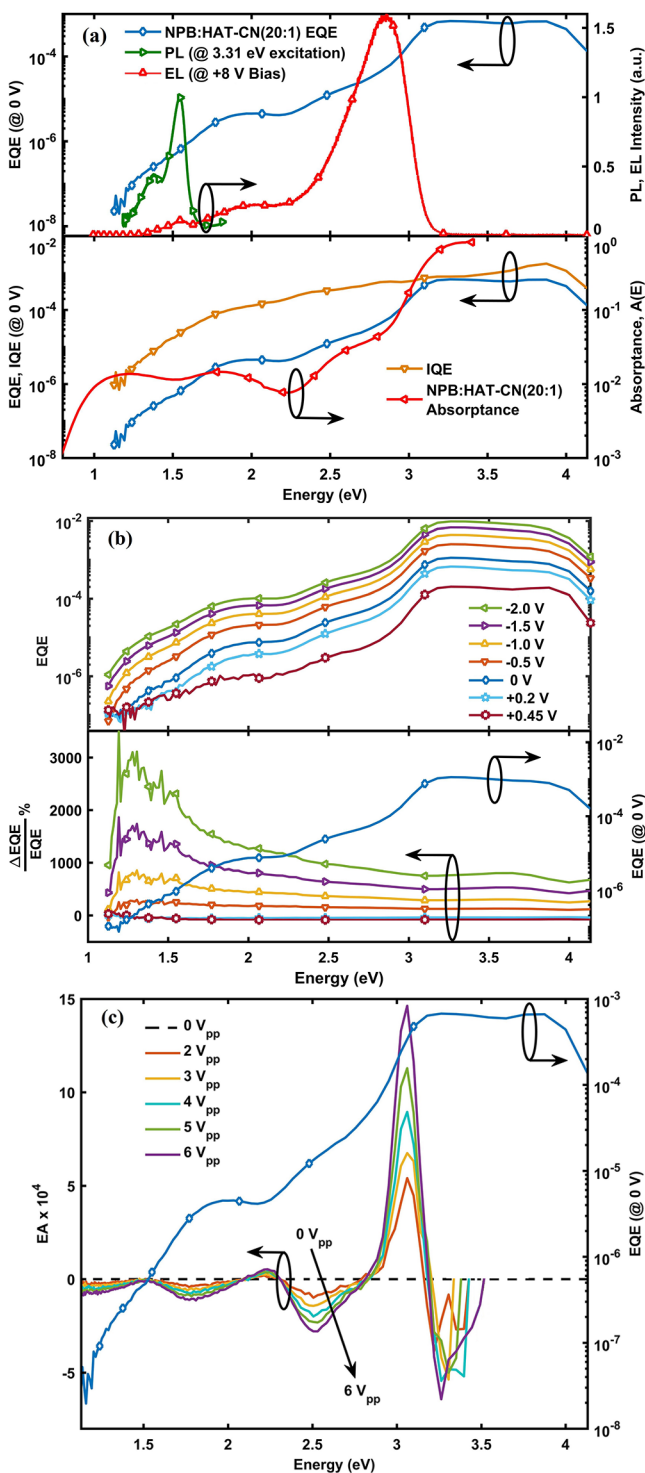
In order to shed light onto the different features appearing in the EQE spectra of NPB:HAT-CN blends, we performed a multiscale modeling analysis combining MD simulations and electronic structure calculations, able to unravel the complex interplay of conformational and environmental effects in disordered heterogeneous blends (see Methods section and Supporting Information for details). Our analysis reveals that these very broad CT features in the EQE spectra result from a combination of three different factors, namely, (i) the presence of three nearly degenerate acceptor levels for the HAT-CN molecule (at the crystalline geometry, the LUMO is 2-fold degenerate and the LUMO+2 lies just 0.16 eV above); (ii) the large fluctuation of NPB molecular energy levels due to conformational effects in the disordered structure; (iii) the variations in the local environment of the molecules resulting in a marked energetic disorder due to intermolecular electrostatic interactions. In particular, in Table S4, we quantified the contributions from intramolecular conformational disorder and electrostatics to broadening of the CT bands.

For an easier comparison with theoretical data, in Figure 3, we show multi-Gaussian fits to the EQE of an NPB:HAT-CN (20:1) device, yielding CT_1 centered at 1.44 eV with a 0.31 eV full width at half-maximum (fwhm), CT_2 at 1.98 eV with a 0.50 eV fwhm, and CT_3 at 2.78 eV with a 0.65 eV fwhm. Given that NPB:HAT-CN(20:1) films are amorphous, multiple CT features in the EQE are unlikely to originate from local morphological heterogeneities in nanocrystalline domains.[9,18,19] Besides the experimental EQE, Figure 3 shows, for an amorphous (20:1) simulated sample, the calculated density of states (DOS) for the two lowest-energy CT excitations (red shaded region for CT_1 and green shaded region for CT_2), which closely match the two lowest energy EQE features. The CT_1 transitions correspond to transitions from the NPB HOMO to the HAT-CN LUMOs, while CT_2

relates to analogous excitations from the NPB HOMO−1 (see sketch in the figure inset). The quantitative difference between the spread of the Gaussian fits of the EQE spectrum and the calculated DOS might be attributed to an energy-dependent absorption intensity, charge separation, and extraction but also to an improper classical treatment of high-frequency vibrational modes.[37] This analysis is further corroborated by time-dependent density functional theory (TD-DFT) calculations on an NPB-HAT-CN dimer extracted from the MD sample (vertical bars), which show two series of absorption bands, CT_1 (red) and CT_2 (green), each of which consists of three transitions to the acceptor HAT-CN LUMO levels. The hole and electron densities of the CT_1 and CT_2 transitions are displayed in the right panels of Figure 3. A precise assignment of the much broader band (3) in the EQE spectrum is less straightforward. In fact, we expect the occurrence of additional higher-energy CT states, corresponding to transitions from deeper levels of NPB or to higher energy unoccupied levels of HAT-CN. These higher-energy CT states are likely to hybridize with localized excitations (LE), which are also expected to produce broad sub-bandgap features at D−A heterojunctions.[17,38] In addition, we cannot exclude a possible contribution from the NPB cation (polaron) around 2.6 eV.

The presence of different electronic CT state features in the EQE provides us with a unique opportunity to study their role in photocurrent generation and recombination. To this end, Figure 4a displays the PL spectrum from a NPB:HAT-CN (20:1) film excited at 3.31 eV (wavelength λ = 375 nm). The spectrum is fitted by two Gaussian functions centered at 1.55 and 1.38 eV (see Figure S4a), respectively having fwhm's of 0.11 and 0.25 eV. The observed spectrum most likely corresponds to the broad CT_2 feature at 2.0 eV in the EQE, considering that typically a reorganization energy of 0.4−0.6 eV exists between absorption (EQE) and emission (PL). The existence of two peaks could be justified as emission from CT_2 to high frequency mode vibrational energy levels of the ground state, which could be assigned to bond vibrations.[29] Surprisingly, no PL is observed for CT features 1 and 3 (cf. Figure 3), as seen from the complete PL spectrum in Figure S4b. Additionally, no PL signals are observed when exciting the film directly into the CT manifold at 1.94 eV (λ = 638 nm), most likely due to the lack of an excited state population manifested by the weak absorption (negligible transition dipole moment) between the ground and CT states. Figure 4a also shows the EL spectrum of the NPB:HAT-CN (20:1) device at a +8 V bias, displaying three distinct emission regions near 2.8, 1.9, and 1.5 eV. The EL spectrum can be fit with Gaussian functions centered at 2.89, 2.69, 2.05, 1.54, and 1.45 eV, respectively having fwhm's of 0.26, 0.43, 0.72, 0.08, and 0.16 eV (Figure S4c). Figure S4d shows EL spectra from the device at voltage biases ranging from +2 V to +8 V. Emissions at 2.89 and 2.69 eV are assigned to the NPB singlet, while emission at 2.05 eV is from CT_3. On the other hand, peaks at 1.54 and 1.45 eV are assigned to emission from CT_2 to ground state vibronic levels, similar to the observed PL spectrum.

The bottom panel of Figure 4a shows the IQE of a 20:1 NPB:HAT-CN blend device calculated from EQE divided by absorption spectrum that is obtained from a transfer matrix model.[39,40] We find that IQE is relatively constant in the Frenkel and high energy CT state absorption regions, while it drops off sharply at energies below 2.3 eV. This suggests inequivalent dissociation and recombination rates among the different CT states in the manifold. Examining EQE with

Figure 4. continued

Electroabsorption signal of an NPB:HAT-CN (20:1) device, measured with 2 to 6 V peak-to-peak sinusoidal AC voltage bias at 1 kHz frequency. The device is kept under a −2 V DC reverse bias to minimize charge injection. The EA signal demonstrates features corresponding to the Stark shift of NPB singlet, CT_3, CT_2, and CT_1 energy states.

applied voltage bias in the range of −2.0 V to +0.45 V in Figure 4b reveals that the lowest energy CT state experiences the largest change with applied reverse bias. To apply reverse bias higher than −2.0 V, we needed to switch to a pulsed voltage source, which allowed us to reach −13.0 V without degrading the device. As seen in Figure S5, the EQE at the lowest energy state continues to increase with higher reverse bias until saturation beyond 10 V. Saturation in the EQE, despite the continual increase in injected current density with applied reverse bias (Figure S3b), supports that the change in lowest energy EQE is not due to an increase in polaron absorption but rather due to increased dissociation efficiency. At sufficiently high reverse bias, almost all low energy excitons are dissociated, and further increases to the bias voltage do not improve EQE. We have also performed electroabsorption (EA) measurements on the NPB:HAT-CN (20:1) device, maintaining the device under a constant reverse bias of −2.0 V and applying an additional 1 kHz sinusoidal voltage to probe the change in absorption. Since the net change in injected current density is zero, the EA spectrum should be free from any polaron signature. From the EA spectrum in Figure 4c, we see features around 3.5−3 eV, 2.8−2.1 eV, 2−1.4 eV, and 1.2 eV that correspond to changes in energy levels of the NPB singlet, CT_3, CT_2, and CT_1 due to the Stark effect, further corroborating our EQE peak assignments in Figure 3. Overall, the EQE measurements under voltage bias indicate that polaron pairs relaxed to the lowest energy CT states do not contribute to photocurrent generation effectively and instead act as a major recombination pathway. Therefore, NPB:HAT-CN (20:1) provides an additional,[9] but not necessarily generalizable, counterexample to the mainstream idea that relaxed CT states contribute equally to photocurrent compared to localized Frenkel excitations or other higher energy CT states.[10]

For efficient solar cells, reciprocity between absorption (EQE) and emission (EL) is observed and can be used to determine the CT energy and reorganization energy (λ_s).[10,23] From the EL and EQE spectra in the top panel of Figure 4a, we can see that reciprocity is maintained for CT_3 and CT_2. However, CT_1 appears to break reciprocity if we consider the EQE measured under short circuit conditions. This is perhaps not surprising, as the CT_1 IQE exhibits a strong photon energy dependence, in violation of one of the assumptions for reciprocity. From Figure 4b, we can see that at a +0.45 V forward bias, CT_1 EQE is severely quenched, which would be even more severe at a +8 V bias, meaning that no photocurrent is expected to be generated from CT_1 at the bias voltage at which EL is measured and voltage dependence of the EQE is needed to be considered, in agreement with a recent proposal about reciprocity.[41] So, in principle, reciprocity still holds in the sense that, with appropriate biasing condition, no emission emerges from a state that does not generate photocurrent.

Finally, we propose the state diagram shown in Figure 5 to explain our collective observations of the NPB:HAT-CN

Figure 4. (a, top) Photoluminescence spectrum of an NPB:HAT-CN (20:1) film excited at 3.31 eV (green solid line), which could be fitted by two distinct Gaussians with peaks located at 1.55 and 1.38 eV (Figure S4a). Electroluminescence spectrum of an NPB:HAT-CN (20:1) device at +8 V bias (red solid line), showing three distinct features with peaks located at approximately 2.8, 1.9, and 1.5 eV. (bottom) Absorptance of a 20:1 NPB:HAT-CN film measured via PDS (red). Estimated IQE (gold) and EQE spectra of an NPB:HAT-CN (20:1) device (blue). The IQE exhibits a 2 orders of magnitude drop from 2.0 to 1.1 eV. (b, top) EQE of a NPB:HAT-CN (20:1) device at different voltage biases ranging from −2 V to +0.45 V. (bottom) Percent change in EQE with applied bias, showing that the lowest energy CT state is most sensitive to applied reverse bias. (c)
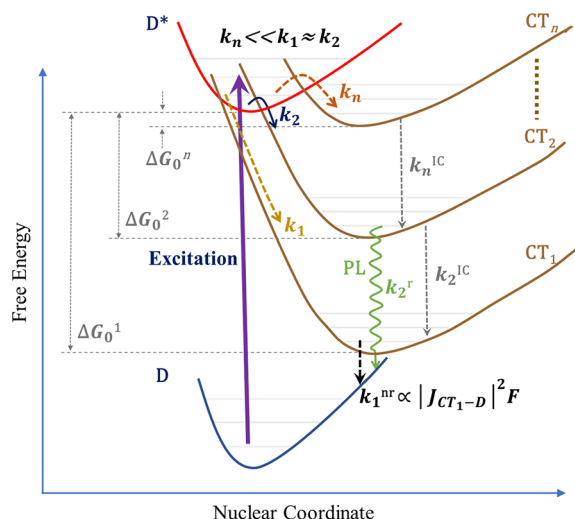
Figure 5. Proposed state diagram of the CT_1, CT_2, and higher energy CT_n electronic levels, along with the ground (D) and excited state (D*) energy levels. ΔG_0^i ($i = 1, 2, ..., n$) is the driving force of the electron transfer to CT_1, CT_2, ..., CT_n, respectively, from D*. Upon excitation of the donor, PL is observed only from CT_2 at a rate k_2^r. This could be explained by assuming that CT_1 is in the Marcus inverted region and CT_n has a large barrier, thus only CT_2 can be populated from a localized intramolecular Frenkel excitation. k_1, k_2, and k_n are charge transfer rates from D* to CT_1, CT_2, and CT_n, respectively, where $k_n \ll k_1 \approx k_2$. k_n^{IC} is the internal conversion rate from the CT_n to CT_{n-1} state. k_2^{IC} has to be smaller than k_2^r, to sustain PL emission from CT_2. k_1^{nr} is the nonradiative recombination rate from the lowest energy CT state (CT_1) to ground states (D), which is proportional to the square of the CT_1-D state electronic coupling, $J_{CT_1\text{-}D}$, and overlap between the CT_1 and ground state vibronic modes, i.e., the Franck-Condon factor (F).

system. The large D−A energy offset leads to a broad sub-bandgap distribution of CT states, which increases the chance, or perhaps even ensures, that the lowest energy CT state falls in the Marcus inverted region and experiences an elevated activation barrier during the transition from the Frenkel (D*) to CT state. High energy CT states (i.e., CT_2, ..., CT_n, where $n = 3, 4, ...$) in the normal Marcus region follow the trend that the activation barrier increases with the CT state energy. The charge transfer rate from D* to CT_1, CT_2, and CT_n, therefore, follows the relationship $k_n \ll k_1 \approx k_2$, where the subscript numbers correspond to the CT state electronic levels. The activation barrier seen by the charge carriers in the D* state is given by $[(\lambda_i + \Delta G_0^i)^2]/[4\lambda_i]$, where ΔG_0^i is the driving force of the charge transfer, λ_i is the reorganization energy, and index i ($= 1, 2, ..., n$) denotes the CT state electronic levels. The driving force ΔG_0^i is directly related to the CT state energy level E_{CT_n} and could be expressed as the energy difference between the relaxed excited-state energy and the CT states (Figure 5). As shown in Figure 3, CT_1 and CT_2 are primarily composed of NPB HOMO to HAT-CN LUMO+1 and NPB HOMO−1 to HAT-CN LUMO transitions, respectively. Internal conversion from CT_2 to CT_1 would require a significant nonadiabatic coupling between the CT_1 and CT_2 potential energy surfaces. The conversion rate is limited by the significant energy separation between the two states and, most importantly, by the different spatial confinement of the CT_2 and CT_1 molecular wave functions, mostly differing for the singly occupied molecular orbital on NPB. Overall, these factors ensure that once CT_2 excitons are formed, the internal

conversion from CT_2 to CT_1 (with rate k_2^{IC}) competes with the radiative recombination (at rate k_2^r) from CT_2 to D (i.e., $k_2^r > k_2^{IC}$), and PL from CT_2 is observed. Furthermore, we speculate that CT_1 is strongly electronically coupled to the ground state ($J_{CT_1\text{-}D}$), which together with a favorable spectral overlap (F, Franck−Condon Factor) due to the small CT_1 state energy results in dominant nonradiative recombination (at rate $k_1^{nr} \propto |J_{CT_1\text{-}D}|^2 F$)[30,33,42] from CT_1 to D, following the usual energy gap law of organic molecules,[33] and no PL emission is observed from this state. The higher energy CT states (CT_n) do not contribute to the PL spectra, as these states are inadequately populated due to their high charge transfer activation barrier with the D* state. On the other hand, when current is injected into the device to measure EL, the energy levels are filled from lowest to highest energies with increasing bias voltage regardless of the charge transfer activation barrier of that state and both CT_2 and CT_3 emit. However, EL from the CT_1 is still absent due to the same dominant nonradiative recombination processes discussed above.

CONCLUSIONS

We have demonstrated several organic D−A interfaces with unconventionally broad CT state features (>2 eV) and performed an in-depth study on NPB:HAT-CN BHJs. The broad CT features in the NPB:HAT-CN system were determined to originate from multiple electronic CT state energies broadened by conformational and dielectric environment heterogeneities. From a device performance standpoint, these devices are, on purpose, far from ideal, as they are incapable of realizing large photocurrent (due to the high donor and acceptor optical gap energies) and V_{OC} (due to very large orbital offset energies and strong nonradiative recombination). However, this heterojunction energetic design has allowed us to explore CT state spectral features over a broad range of photon energies, to probe their properties in ways not feasible in other D−A systems and to better learn about the role of CT states in energy loss and charge generation. In the NPB:HAT-CN example that we studied in detail, ultrasensitive absorption measurement revealed low energy CT states, which are not evident from EQE measurements. The estimated IQE of the device, along with the voltage bias dependent EQE, revealed that carrier dissociation efficiency in these devices is strongly photon energy dependent and that the low energy CT state suffers from severe recombination, owing to a combination of strong electronic coupling and vibronic modes overlapping with the ground state. While most of the current studies in the literature involving charge generation and a recombination mechanism through CT states are done on archetypal high-performance material systems, a further in-depth study of the large frontier orbital energy offset materials discussed in this work could provide us an alternate path of investigation from the opposite end of the performance spectrum unraveling crucial information about the full extent of such CT-mediated loss mechanisms and help us construct design rules that would be useful for designing the next generation of high performance solar cells.

METHODS

Device and Film Preparation. All materials were purchased from commercial vendors: Bathocuproine (BCP; Lumtec), NPB (Nichem), m-TDATA (Sigma-Aldrich), NTCDA (TCI America),

TAPC (Lumtec), TPD (Lumtec), HAT-CN (Nichem), and PVK (Sigma-Aldrich). NPB, m-TDATA, and NTCDA were purified via thermal gradient sublimation prior to use, whereas other materials were used as received.

Prepatterned ITO glass substrates (Colorado Concept Coatings) were used for solar cells. Quartz (AdValue Technology) substrates were used for absorption and PL measurements. All substrates were cleaned by successive sonication in deionized water (40 °C, 15 min), acetone (40 °C, 10 min), and isopropanol (40 °C, 10 min), followed by oxygen plasma treatment for 10 min.

The small molecule devices were fabricated using thermal evaporation with ~10^{-7} Torr base pressure. The basic structure of the devices was ITO/donor:acceptor/BCP (8−10 nm)/Al (100 nm). All active layers of the devices and the films ranged from 40 to 150 nm in thickness. The small molecule organic donor materials were coevaporated with the acceptor materials, to make a bulk heterojunction (BHJ). Since the acceptor NTCDA tends to crystallize,[43] its volume fraction was kept small to ensure a disordered film morphology. As for HAT-CN, although the vacuum deposited films do not suffer from crystallization,[44] the volume ratio was kept relatively low to avoid any aggregation or crystallization induced effects. We have fabricated BHJ devices with NPB:HAT-CN (20:1), NPB:NTCDA (10:1), TAPC:HAT-CN (20:1), m-TDATA:NTCDA (10:1), and TPD:HAT-CN (20:1) bulk active layers, where the blend ratio denotes mixing of the donor and acceptor materials by volume.

For the polymer donor PVK, planar heterojunction (PHJ) devices were formed with HAT-CN by solution processing, due to the lack of a suitable common solvent for PVK and HAT-CN. We have deposited HAT-CN by both solution processing and vacuum deposition, with both devices producing the same broad sub-bandgap EQE spectrum (Figure S6). To make devices, PEDOT:PSS (Heraeus) was spin-coated on cleaned ITO-glass substrates at 5000 rpm for 60 s, followed by a 20 min annealing at 140 °C. PVK films were formed by spin coating 5 mg/mL solution (in chlorobenzene (Sigma-Aldrich)) at 1000 rpm for 60 s. The HAT-CN layer was formed by spin coating from a 5 mg/mL solution as well (in acetonitrile (Sigma-Aldrich)), at 2000 rpm for 30 s. Films were annealed at 150 °C, for 20 min. The entire active layer preparation was done in a N_2 filled glovebox and later transferred to a thermal deposition chamber for depositing BCP and Al contact on top of the films. The active area of all devices was 0.1 cm^2.

IV and EQE Characterization. The current−voltage characteristics of the solar cells were measured using a solar simulator (ABET Technologies) calibrated for 1 sun AM1.5G illumination and a Keithley 2400 source meter. The EQE measurements were taken using a Newport TLS-300X tunable light source under short-circuit conditions unless otherwise noted. The monochromatic light output from the light source was chopped at 390 Hz using an optical chopper. Device photocurrent was amplified by a current preamplifier (SR570, Stanford Research Systems) and detected by a lock-in amplifier (SR830, Stanford Research Systems) tuned to the optical chopper frequency. To count the number of incoming photons from the light source, calibrated Si and Ge photodiodes from Newport were used as reference cells.

EQE Under Voltage Bias. External voltage bias was applied to the solar cell using a current preamplifier (SR570). To avoid signal overload at the preamplifier output, the applied voltage was kept under a −2 V reverse and +0.45 V forward bias. The preamplifier was operated in low noise mode and a 300 Hz to 1 kHz bandpass filter was applied to the incoming signal. The preamplifier gain was set to 100 nA/V throughout the EQE measurement. For pulsed voltage bias measurements, square wave reverse biases ranging from 0 to 13 V were applied using a Tektronix CFG253 function generator. The applied square wave had a frequency of 1 kHz and a duty cycle of 50%.

Low Temperature V_{OC} Measurement. Low temperature V_{OC} was measured by placing the device inside a Janis VNF-100 Cryostat. The temperature of the device was monitored and controlled by a LakeShore 335 Cryogenic Temperature Controller. A Newport 250-W QTH lamp was calibrated to 1 sun relative intensity to illuminate

the device, and the current−voltage characteristics were measured using a Keithley 2400 source meter. Measurements were done by first cooling down the sample to 80 K and then gradually heating up to the room temperature. No sign of device degradation was observed due to this cool down and heating up process.

Photoluminescence Measurement. Photoluminescence was collected from a NPB:HAT-CN (20:1) blend film excited using a continuous-wave, λ = 375 nm (3.31 eV) excitation laser and a Horiba iHR fiber-coupled spectrometer with a cooled Si CCD array detector.

Electroluminescence Measurement. Electroluminescence spectra were measured with a SpectraPro HRS-300 spectrometer and a PIX-400B charge-coupled device from Princeton Instruments. Forward bias on the device was applied using a Tektronix CFG253 function generator.

Surface Morphology Measurement. The surface morphologies of 100 nm thick NPB:HAT-CN 20:1 and 1:2 films were imaged with a Veeco Dimension 3100 AFM in tapping mode.

Photothermal Deflection Spectroscopy. Photothermal deflection spectroscopy measurements were taken using a 150 W xenon lamp equipped with a three-grating monochromator. Samples were immersed in Fluorinert FC-72 (C_6F_{14}), a liquid with a strongly temperature-dependent refractive index, which equals 1.25 at room temperature. Absorption is measured based on the deflection of a laser beam (JDSU 1137P, 7.0 mW, 632.8 nm neon−helium, linear polarized) by thermally induced changes in the refractive index of the liquid in which the illuminated sample is immersed. The PDS spectra were calibrated to absolute absorptance scale by matching with the UV−vis absorption spectra at 3.18 eV, measured by a PerkinElmer 950 spectrophotometer using an integrating sphere.

Internal Quantum Efficiency Calculation. The absorption $a(E)$ of the D:A blend in a full device comprising glass/ITO/D:A/BCP/Al was calculated using a transfer matrix model[39] where parasitic absorption and optical interference effects are considered. The light was incident normal to the substrate via the ITO anode side. The optical constants (n, k) and thickness of each layer in the model were all measured by ellipsometry, except that k of the D:A layer was obtained from PDS absorptance data, ensuring clearly resolved CT state features. The IQE was then given by EQE/($a(E)$).

Electroabsorption Measurement. Electroabsorption was done on the same NPB:HAT-CN (20:1) devices used for EQE measurements. Monochromatic light was shined through the transparent electrode of the device, and direct reflected light from the Al back contact was collected using a Si photodetector (Newport). The sample was biased with a −2 V DC bias, to prevent any charge injection. Superimposed on the DC bias, a 1 kHz AC sinusoidal voltage with peak-to-peak values from 2 to 6 V was applied. The difference in photocurrent in the Si detector due to the reflected light from the NPB:HAT-CN device at different applied AC voltages was measured using a lock-in amplifier (SR830).

Molecular Dynamics Simulations. A film of 9:1 NPB:HAT-CN m/m ratio (about 13:1 in weight, 20:1 in volume) was prepared by vapor codeposition on graphene by means of NVT nonequilibrium molecular dynamics (MD) simulations[45,46] for a final thickness exceeding 100 Å. The system was modeled with a previously developed united atom force field.[47] United atom charges were obtained by fitting the electrostatic potential at the optimized geometry calculated at the DFT PBE0[48]/def2-TZVP level of theory. A horizontal graphene surface of 76.14 Å × 76.57 Å was chosen as a simple rigid support and kept fixed during the simulations, with a vertical box dimension of 400 Å. Deposition proceeded by randomly selecting the chemical species of the new molecule to be added at each step, according to the desired molar ratio. Every new molecule was placed at about 20 Å above the forming organic layer, endowed with a velocity of 1 Å ps^{-1} directed toward the graphene surface; then the dynamic of the system evolved for 100 ps at 500 K. In the case of desorption, the step was repeated without randomizing again the molecular species. The final composition of the sample was of 897 NPB and 103 HAT-CN molecules. The adopted scheme yielded an amorphous sample, as verified by inspecting radial distributions, linear mass density along the box sides, and orientational order parameters.

The system was subsequently equilibrated at 300 K for at least 60 ns, and the final configuration was used to extract the molecular geometries for the calculations of electronic properties.

Electronic Structure Calculations. The DOS of CT states in Figure 3 were calculated upon sampling over molecular conformations obtained from MD simulations. CT states' energies were computed for all the NPB-HAT-CN dimers of the inner, bulk-like region of the MD-deposited film as

$$E_{CT} = E_A - E_D + \Delta^{\pm} \tag{1}$$

where $E_A = E_{L+i}$ and $E_D = E_{H-j}$ are the gas-phase energies of the HAT-CN LUMO+i ($i = 0, 1, 2$) and of the NPB HOMO-j ($j = 0, 1$) orbitals, respectively. $\Delta^{\pm}$ is the ion pair polarization energies that accounts for the electron−hole Coulomb attraction and environmental effects in the disordered blend. The latter was computed from self-consistent MicroElectrostatic calculations as implemented in the MESCAL code.[49]

Gas-phase energy levels were calculated combining evGW calculations, ensuring very accurate absolute values, and DFT, allowing the sampling of molecular conformations and of the corresponding energy level fluctuations. The energy of a generic energy level k reads:

$$E_k(r_{MD}) = E_k^{GW}(r_0) + [E_k^{DFT}(r_{MD}) - E_k^{DFT}(r_0)] \tag{2}$$

where r_{MD} labels the geometry of a given molecule in the MD sample and r_0 is a reference geometry, taken from the bulk crystal structure of both species. evGW calculations (PBE0[48] functional, complete basis set limit) were performed with the Fiesta code.[50,51] DFT energy levels were computed at the ωB97X-D[52]/6-311++G(d,p) level.

TD-DFT calculations were performed for NPB-HAT-CN dimers extracted from the MD sample at the CAM-B3LYP[53]/6-31G(d,p) level, accounting for a continuum polarizable[54] embedding with dielectric constant $\varepsilon_r = 3$. DFT and TD-DFT calculations were carried out with the Gaussian 16[55] suite.

■ ASSOCIATED CONTENT

Ⓢ Supporting Information

The Supporting Information is available free of charge on the ACS Publications website at DOI: 10.1021/acs.chemmater.9b01279.

> Molecular structures and energetics of organic materials used, absorption and EQE spectra of doped NPB, current density−voltage characteristics (both dark and under illumination) and open-circuit voltage for different NPB:HAT-CN blends, complete PL and EL spectra of NPB:HAT-CN(20:1), EQE spectra under pulsed voltage bias, EQE of PVK/HAT-CN planar devices, details on electronic structure calculations, energy level distribution of NPB and HAT-CN frontier orbitals, CT states energy distributions, and absorption spectra of NPB-HAT-CN dimers (PDF)

■ AUTHOR INFORMATION

Corresponding Author

*E-mail: brand@princeton.edu.

ORCID Ⓞ

Gabriele D'Avino: 0000-0002-5897-2924
Luca Muccioli: 0000-0001-9227-1059
Noel C. Giebink: 0000-0002-3798-5830
David Beljonne: 0000-0002-2989-3557
Barry P. Rand: 0000-0003-4409-8751

Notes

The authors declare no competing financial interest.

■ REFERENCES

(1) Green, M. A.; Hishikawa, Y.; Dunlop, E. D.; Levi, D. H.; Hohl-Ebinger, J.; Yoshita, M.; Ho-Baillie, A. W. Y. Solar Cell Efficiency Tables (Version 53). *Prog. Photovoltaics* **2019**, *27*, 3−12.

(2) Gao, F.; Inganäs, O. Charge Generation in Polymer−Fullerene Bulk-Heterojunction Solar Cells. *Phys. Chem. Chem. Phys.* **2014**, *16*, 20291−20304.

(3) Clarke, T. M.; Durrant, J. R. Charge Photogeneration in Organic Solar Cells. *Chem. Rev.* **2010**, *110*, 6736−6767.

(4) Vandewal, K.; Tvingstedt, K.; Gadisa, A.; Inganäs, O.; Manca, J. V. On the Origin of the Open-Circuit Voltage of Polymer−Fullerene Solar Cells. *Nat. Mater.* **2009**, *8*, 904−909.

(5) Linderl, T.; Zechel, T.; Brendel, M.; Moseguí González, D.; Müller-Buschbaum, P.; Pflaum, J.; Brütting, W. Energy Losses in Small-Molecule Organic Photovoltaics. *Adv. Energy Mater.* **2017**, *7*, 1700237.

(6) Burke, T. M.; Sweetnam, S.; Vandewal, K.; McGehee, M. D. Beyond Langevin Recombination: How Equilibrium Between Free Carriers and Charge Transfer States Determines the Open-Circuit Voltage of Organic Solar Cells. *Adv. Energy Mater.* **2015**, *5*, 1500123.

(7) Grancini, G.; Maiuri, M.; Fazzi, D.; Petrozza, A.; Egelhaaf, H.-J.; Brida, D.; Cerullo, G.; Lanzani, G. Hot Exciton Dissociation in Polymer Solar Cells. *Nat. Mater.* **2013**, *12*, 29−33.

(8) Ohkita, H.; Cook, S.; Astuti, Y.; Duffy, W.; Tierney, S.; Zhang, W.; Heeney, M.; McCulloch, I.; Nelson, J.; Bradley, D. D. C.; et al. Charge Carrier Formation in Polythiophene/Fullerene Blend Films Studied by Transient Absorption Spectroscopy. *J. Am. Chem. Soc.* **2008**, *130*, 3030−3042.

(9) Liu, X.; Ding, K.; Panda, A.; Forrest, S. R. Charge Transfer States in Dilute Donor−Acceptor Blend Organic Heterojunctions. *ACS Nano* **2016**, *10*, 7619−7626.

(10) Vandewal, K.; Albrecht, S.; Hoke, E. T.; Graham, K. R.; Widmer, J.; Douglas, J. D.; Schubert, M.; Mateker, W. R.; Bloking, J. T.; Burkhard, G. F.; et al. Efficient Charge Generation by Relaxed Charge-Transfer States at Organic Interfaces. *Nat. Mater.* **2014**, *13*, 63−68.

(11) Lee, J.; Vandewal, K.; Yost, S. R.; Bahlke, M. E.; Goris, L.; Baldo, M. A.; Manca, J. V.; Van Voorhis, T. Charge Transfer State Versus Hot Exciton Dissociation in Polymer-Fullerene Blended Solar Cells. *J. Am. Chem. Soc.* **2010**, *132*, 11878−11880.

(12) Sánchez-Carrera, R. S.; Paramonov, P.; Day, G. M.; Coropceanu, V.; Brédas, J.-L. Interaction of Charge Carriers with Lattice Vibrations in Oligoacene Crystals from Naphthalene to Pentacene. *J. Am. Chem. Soc.* **2010**, *132*, 14437−14446.

(13) Tummala, N. R.; Zheng, Z.; Aziz, S. G.; Coropceanu, V.; Brédas, J.-L. Static and Dynamic Energetic Disorders in the C_{60}, $PC_{61}BM$, C_{70}, and $PC_{71}BM$ Fullerenes. *J. Phys. Chem. Lett.* **2015**, *6*, 3657−3662.

(14) Unger, T.; Wedler, S.; Kahle, F.-J.; Scherf, U.; Bässler, H.; Köhler, A. The Impact of Driving Force and Temperature on the Electron Transfer in Donor−Acceptor Blend Systems. *J. Phys. Chem. C* **2017**, *121*, 22739−22752.

(15) Tummala, N. R.; Elroby, S. A.; Aziz, S. G.; Risko, C.; Coropceanu, V.; Brédas, J.-L. Packing and Disorder in Substituted Fullerenes. *J. Phys. Chem. C* **2016**, *120*, 17242−17250.

(16) Belova, V.; Beyer, P.; Meister, E.; Linderl, T.; Halbich, M.-U.; Gerhard, M.; Schmidt, S.; Zechel, T.; Meisel, T.; Generalov, A. V.; et al. Evidence for Anisotropic Electronic Coupling of Charge Transfer States in Weakly Interacting Organic Semiconductor Mixtures. *J. Am. Chem. Soc.* **2017**, *139*, 8474−8486.

(17) Chen, X.-K.; Coropceanu, V.; Brédas, J.-L. Assessing the Nature of the Charge-Transfer Electronic States in Organic Solar Cells. *Nat. Commun.* **2018**, *9*, 5295.

(18) Lin, Y. L.; Zhang, F.; Kerner, R. A.; Yang, T. C.-J.; Kahn, A.; Rand, B. P. Variable Charge Transfer State Energies at Nano-structured Pentacene/C_{60} Interfaces. *Appl. Phys. Lett.* **2018**, *112*, 213302.

(19) Lin, Y. L.; Fusella, M. A.; Rand, B. P. The Impact of Local Morphology on Organic Donor/Acceptor Charge Transfer States. *Adv. Energy Mater.* **2018**, *8*, 1702816.

(20) Ding, K.; Liu, X.; Forrest, S. R. Charge Transfer and Collection in Dilute Organic Donor−Acceptor Heterojunction Blends. *Nano Lett.* **2018**, *18*, 3180−3184.

(21) Roland, S.; Kniepert, J.; Love, J. A.; Negi, V.; Liu, F.; Bobbert, P.; Melianas, A.; Kemerink, M.; Hofacker, A.; Neher, D. Equilibrated Charge Carrier Populations Govern Steady-State Nongeminate Recombination in Disordered Organic Solar Cells. *J. Phys. Chem. Lett.* **2019**, *10*, 1374−1381.

(22) Rau, U. Reciprocity Relation between Photovoltaic Quantum Efficiency and Electroluminescent Emission of Solar Cells. *Phys. Rev. B: Condens. Matter Mater. Phys.* **2007**, *76*, 085303.

(23) Vandewal, K.; Tvingstedt, K.; Gadisa, A.; Inganäs, O.; Manca, J. V. Relating the Open-Circuit Voltage to Interface Molecular Properties of Donor:Acceptor Bulk Heterojunction Solar Cells. *Phys. Rev. B: Condens. Matter Mater. Phys.* **2010**, *81*, 125204.

(24) Brigeman, A. N.; Fusella, M. A.; Rand, B. P.; Giebink, N. C. Nonthermal Site Occupation at the Donor-Acceptor Interface of Organic Solar Cells. *Phys. Rev. Appl.* **2018**, *10*, 034034.

(25) Ma, H.; Troisi, A. Direct Optical Generation of Long-Range Charge-Transfer States in Organic Photovoltaics. *Adv. Mater.* **2014**, *26*, 6163−6167.

(26) Brigeman, A. N.; Fusella, M. A.; Yan, Y.; Purdum, G. E.; Loo, Y.-L.; Rand, B. P.; Giebink, N. C. Revealing the Full Charge Transfer State Absorption Spectrum of Organic Solar Cells. *Adv. Energy Mater.* **2016**, *6*, 1601001.

(27) Dimitrov, S. D.; Bakulin, A. A.; Nielsen, C. B.; Schroeder, B. C.; Du, J.; Bronstein, H.; McCulloch, I.; Friend, R. H.; Durrant, J. R. On the Energetic Dependence of Charge Separation in Low-Band-Gap Polymer/Fullerene Blends. *J. Am. Chem. Soc.* **2012**, *134*, 18189−18192.

(28) Dimitrov, S. D.; Durrant, J. R. Materials Design Considerations for Charge Generation in Organic Solar Cells. *Chem. Mater.* **2014**, *26*, 616−630.

(29) Benduhn, J.; Tvingstedt, K.; Piersimoni, F.; Ullbrich, S.; Fan, Y.; Tropiano, M.; McGarry, K. A.; Zeika, O.; Riede, M. K.; Douglas, C. J.; Barlow, S.; Marder, S. R.; Neher, D.; Spoltore, D.; Vandewal, K. Intrinsic Non-Radiative Voltage Losses in Fullerene-Based Organic Solar Cells. *Nat. Energy* **2017**, *2*, 17053.

(30) Azzouzi, M.; Yan, J.; Kirchartz, T.; Liu, K.; Wang, J.; Wu, H.; Nelson, J. Nonradiative Energy Losses in Bulk-Heterojunction Organic Photovoltaics. *Phys. Rev. X* **2018**, *8*, 031055.

(31) Azzouzi, M.; Kirchartz, T.; Nelson, J. Factors Controlling Open-Circuit Voltage Losses in Organic Solar Cells. *Trends Chem.* **2019**, *1*, 49−62.

(32) Qian, D.; Zheng, Z.; Yao, H.; Tress, W.; Hopper, T. R.; Chen, S.; Li, S.; Liu, J.; Chen, S.; Zhang, J.; et al. Design Rules for Minimizing Voltage Losses in High-Efficiency Organic Solar Cells. *Nat. Mater.* **2018**, *17*, 703−709.

(33) Köhler, A.; Bässler, H. *Electronic Processes in Organic Semiconductors*; Wiley-VCH Verlag GmbH & Co. KGaA: Weinheim, Germany, 2015.

(34) Marchetti, A. P.; Sassin, K. E.; Young, R. H.; Rothberg, L. J.; Kondakov, D. Y. Integer Charge Transfer States in Organic Light-Emitting Diodes: Optical Detection of Hole Carriers at the Anode|organic Interface. *J. Appl. Phys.* **2011**, *109*, 013709.

(35) Buchaca-Domingo, E.; Vandewal, K.; Fei, Z.; Watkins, S. E.; Scholes, F. H.; Bannock, J. H.; de Mello, J. C.; Richter, L. J.; DeLongchamp, D. M.; Amassian, A.; et al. Direct Correlation of Charge Transfer Absorption with Molecular Donor:Acceptor Interfacial Area via Photothermal Deflection Spectroscopy. *J. Am. Chem. Soc.* **2015**, *137*, 5256−5259.

(36) Vandewal, K.; Widmer, J.; Heumueller, T.; Brabec, C. J.; McGehee, M. D.; Leo, K.; Riede, M.; Salleo, A. Increased Open-Circuit Voltage of Organic Solar Cells by Reduced Donor-Acceptor Interface Area. *Adv. Mater.* **2014**, *26*, 3839−3843.

(37) Vandewal, K.; Benduhn, J.; Schellhammer, K. S.; Vangerven, T.; Rückert, J. E.; Piersimoni, F.; Scholz, R.; Zeika, O.; Fan, Y.; Barlow, S.; et al. Absorption Tails of Donor:C_{60} Blends Provide Insight into Thermally Activated Charge-Transfer Processes and Polaron Relaxation. *J. Am. Chem. Soc.* **2017**, *139*, 1699−1704.

(38) D'Avino, G.; Muccioli, L.; Olivier, Y.; Beljonne, D. Charge Separation and Recombination at Polymer−Fullerene Heterojunctions: Delocalization and Hybridization Effects. *J. Phys. Chem. Lett.* **2016**, *7*, 536−540.

(39) Peumans, P.; Yakimov, A.; Forrest, S. R. Small Molecular Weight Organic Thin-Film Photodetectors and Solar Cells. *J. Appl. Phys.* **2003**, *93*, 3693−3723.

(40) Armin, A.; Velusamy, M.; Wolfer, P.; Zhang, Y.; Burn, P. L.; Meredith, P.; Pivrikas, A. Quantum Efficiency of Organic Solar Cells: Electro-Optical Cavity Considerations. *ACS Photonics* **2014**, *1*, 173−181.

(41) Toprasertpong, K.; Delamarre, A.; Nakano, Y.; Guillemoles, J.-F.; Sugiyama, M. Generalized Reciprocity Relations in Solar Cells with Voltage-Dependent Carrier Collection: Application to p - i - n Junction Devices. *Phys. Rev. Appl.* **2019**, *11*, 024029.

(42) Chen, X.-K.; Ravva, M. K.; Li, H.; Ryno, S. M.; Brédas, J.-L. Effect of Molecular Packing and Charge Delocalization on the Nonradiative Recombination of Charge-Transfer States in Organic Solar Cells. *Adv. Energy Mater.* **2016**, *6*, 1601325.

(43) Blackburn, A. C.; Fitzgerald, L. J.; Gerkin, R. E. 1,4,5,8-Naphthalenetetracarboxylic Acid Cyclic 1,8-Anhydride Bis(Dimethyl Sulfoxide) Solvate and 1,4,5,8-Naphthalenetetracarboxylic 1,8:4,5-Dianhydride. *Acta Crystallogr., Sect. C: Cryst. Struct. Commun.* **1997**, *53*, 1991−1995.

(44) Wang, B.; Zhang, L.; Hu, Y.; Shi, X.-B.; Wang, Z.-K.; Liao, L.-S. Doped Hole Injection Bilayers for Solution Processable Blue Phosphorescent Organic Light-Emitting Diodes. *J. Mater. Chem. C* **2016**, *4*, 6570−6574.

(45) D'Avino, G.; Muccioli, L.; Zannoni, C. From Chiral Islands to Smectic Layers: A Computational Journey Across Sexithiophene Morphologies on C_{60}. *Adv. Funct. Mater.* **2015**, *25*, 1985−1995.

(46) Roscioni, O. M.; D'Avino, G.; Muccioli, L.; Zannoni, C. Pentacene Crystal Growth on Silica and Layer-Dependent Step-Edge Barrier from Atomistic Simulations. *J. Phys. Chem. Lett.* **2018**, *9*, 6900−6906.

(47) Moral, M.; Son, W.-J.; Sancho-García, J. C.; Olivier, Y.; Muccioli, L. Cost-Effective Force Field Tailored for Solid-Phase

Simulations of OLED Materials. *J. Chem. Theory Comput.* **2015**, *11*, 3383−3392.

(48) Adamo, C.; Barone, V. Toward Reliable Density Functional Methods without Adjustable Parameters: The PBE0Model. *J. Chem. Phys.* **1999**, *110*, 6158−6170.

(49) D'Avino, G.; Muccioli, L.; Zannoni, C.; Beljonne, D.; Soos, Z. G. Electronic Polarization in Organic Crystals: A Comparative Study of Induced Dipoles and Intramolecular Charge Redistribution Schemes. *J. Chem. Theory Comput.* **2014**, *10*, 4959−4971.

(50) Blase, X.; Attaccalite, C.; Olevano, V. First-Principles GW Calculations for Fullerenes, Porphyrins, Phtalocyanine, and Other Molecules of Interest for Organic Photovoltaic Applications. *Phys. Rev. B: Condens. Matter Mater. Phys.* **2011**, *83*, 115103.

(51) Li, J.; Duchemin, I.; Roscioni, O. M.; Friederich, P.; Anderson, M.; Da Como, E.; Kociok-Köhn, G.; Wenzel, W.; Zannoni, C.; Beljonne, D.; et al. Host Dependence of the Electron Affinity of Molecular Dopants. *Mater. Horiz.* **2019**, *6*, 107−114.

(52) Chai, J.-D.; Head-Gordon, M. Long-Range Corrected Hybrid Density Functionals with Damped Atom−Atom Dispersion Corrections. *Phys. Chem. Chem. Phys.* **2008**, *10*, 6615−6620.

(53) Yanai, T.; Tew, D. P.; Handy, N. C. A New Hybrid Exchange−Correlation Functional Using the Coulomb-Attenuating Method (CAM-B3LYP). *Chem. Phys. Lett.* **2004**, *393*, 51−57.

(54) Tomasi, J.; Mennucci, B.; Cammi, R. Quantum Mechanical Continuum Solvation Models. *Chem. Rev.* **2005**, *105*, 2999−3094.

(55) Frisch, M. J.; Trucks, G. W.; Schlegel, H. B.; Scuseria, G. E.; Robb, M. A.; Cheeseman, J. R.; Scalmani, G.; Barone, V.; Petersson, G. A.; Nakatsuji, H.; Li, X.; Caricato, M.; Marenich, A. V.; Bloino, J.; Janesko, B. G.; Gomperts, R.; Mennucci, B.; Hratchian, H. P.; Ortiz, J. V.; Izmaylov, A. F.; Sonnenberg, J. L.; Williams-Young, D.; Ding, F.; Lipparini, F.; Egidi, F.; Goings, J.; Peng, B.; Petrone, A.; Henderson, T.; Ranasinghe, D.; Zakrzewski, V. G.; Gao, J.; Rega, N.; Zheng, G.; Liang, W.; Hada, M.; Ehara, M.; Toyota, K.; Fukuda, R.; Hasegawa, J.; Ishida, M.; Nakajima, T.; Honda, Y.; Kitao, O.; Nakai, H.; Vreven, T.; Throssell, K.; Montgomery, J. A., Jr.; Peralta, J. E.; Ogliaro, F.; Bearpark, M. J.; Heyd, J. J.; Brothers, E. N.; Kudin, K. N.; Staroverov, V. N.; Keith, T. A.; Kobayashi, R.; Normand, J.; Raghavachari, K.; Rendell, A. P.; Burant, J. C.; Iyengar, S. S.; Tomasi, J.; Cossi, M.; Millam, J. M.; Klene, M.; Adamo, C.; Cammi, R.; Ochterski, J. W.; Martin, R. L.; Morokuma, K.; Farkas, O.; Foresman, J. B.; Fox, D. J. *Gaussian 16*, Revision A.03; Gaussian, Inc.: Wallingford, CT, 2016.